Hindawi
International Journal of Antennas and Propagation
Volume 2022, Article ID 1741454, 14 pages
https://doi.org/10.1155/2022/1741454

Research Article

Analysis, Optimization, and Hardware Implementation of Dipole Antenna Array for Wireless Applications

Norun Abdul Malek,[1] **Rob D. Seager**,[2] **James A. Flint**,[2] **and Zuhairiah Zainal Abidin**[3]

[1]*Microwave, Communication and Information System Engineering Research Group, International Islamic University Malaysia, Jalan Gombak, 53100, Kuala Lumpur, Malaysia*
[2]*Wolfson School of Mechanical, Electrical and Manufacturing Engineering, Loughborough University, Leicestershire, UK*
[3]*Advanced Telecommunication Research Center (ATRC), Faculty of Electrical and Electronics Engineering, Universiti Tun Hussein Onn Malaysia, Parit Raja 86400, Batu Pahat, Malaysia*

Correspondence should be addressed to Norun Abdul Malek; norun@iium.edu.my

Received 17 January 2022; Accepted 24 June 2022; Published 30 August 2022

Academic Editor: Francesco D'Agostino

Copyright © 2022 Norun Abdul Malek et al. This is an open access article distributed under the Creative Commons Attribution License, which permits unrestricted use, distribution, and reproduction in any medium, provided the original work is properly cited.

The antenna pattern synthesis is one of the significant problems in the phased array antenna. Pattern synthesis refers to the optimized weight excitation of each antenna element in order to steer the beam electronically without mechanically rotating the antenna. It can be achieved by using a combination of phase shifters and attenuator circuits. In this paper, a 2 by 2 dipole antennas with an RF beamforming circuit has been designed to steer the main beam along the azimuth plane. The main beam coverage from 100° to 140° with a step size of 10° has been successfully optimized using a hybrid of the induced EMF method and a genetic algorithm. The optimization results were compared to the full-wave simulation technique implemented in Empire XCCel. The design is realistically implemented at 2.45 GHz, with both simulation and measurement results shown. The measured reflection coefficient of the phased array antenna is −48 dB at 2.56 GHz. The feasibility of the beam synthesis has been validated successfully with the main beam being steered at 110°. The possibility of a fabrication discrepancy resulting in minor radiation degradation is also discussed in this research. The dipole antenna system with RF beamformer circuit can be applied to indoor positioning systems such as Wi-Fi, wireless local area network (WLAN), and fifth-generation.

1. Introduction

In recent years, adaptive beamforming has gained high interest due to the rollout of 5G technology. The advantages of 5G technology include a wide band spectrum, low latency, and high speed, which is around 1 Gb/s. However, the challenges of shifting the existing band to a higher mm-wave will increase the path loss according to Friis' equation. Research studies [1] have presented the outdoor path loss model for New York City at 28 GHz and 73 GHz. It has been reported that the path loss at higher mm-wave frequencies ranges between 20 dB and 25 dB in comparison to the existing cellular systems.

On top of that, the radio propagation channel at high frequencies in tropical countries is facing substantial losses due to rainfall intensity and rain attenuation. For example, research studies [2] have presented rain attenuation in Malaysia at high frequencies (21.8 GHz and 70.5 GHz) up to 40 dB for 1.8 km links with a maximum rain rate of 108 mm/h.

In order to mitigate these challenges, large-scale antenna arrays (LSAAs) with intelligent signal processing, including beamforming, have been proposed in several studies [3–7]. The improvement includes enhanced spectral efficiency, high gain, and reduced interference at mm-waves.

Beamforming refers to a signal processing technique to concentrate the transmitting power into specific beams between the transmitter and the receiver while placing nulls in the direction of interferers. This technique can be achieved by using a large number of antennas to send similar

signals of varying amplitudes and phases from multiple transmitters. Conventional techniques employ omnidirectional antennas at the base station, where the antennas can extend the signal equally in all directions. However, beamforming can be applied and exploited at mm-waves due to the small size of the antennas at high frequencies, thus enabling the possibility of massive antennas in MIMO and LSAS becoming a reality [8].

Many recent kinds of research work investigate the channel performance using analog beamforming [9–11]. Other works [12] investigate the use of a hybrid-dual polarized antenna to enhance the energy efficiency of UAVs. While [13] has demonstrated a 5G MIMO antenna with high isolation between the four elements. However, this research investigates antenna array configurations rather than focusing on the performance of analog beamforming or antenna design. Many researchers investigate analog beamforming algorithms in terms of array performance [14–21]. To date, there has been a lack of discussion in terms of the hardware implementation of the effectiveness of the proposed methods by the measurement results. Even though [14, 15, 21] they are hardware implementations, the optimization method, type of antennas, and objective functions are different compared to this research.

This paper investigates the antenna array and RF beamforming techniques in the context of analysis, optimization, and experimental setup using 2 by 2 dipole antennas at 2.45 GHz. The reason of the frequency selection is due to the low cost and the convenience of the RF beamformer circuit (attenuator and phase shifter SMD) at 2.45 GHz. Section 2 describes the radiation pattern analysis using the induced EMF method in order to calculate the total radiation pattern, including the mutual coupling of the dipole antenna array. Furthermore, an optimization technique using a genetic algorithm (GA) is used to steer the main beam towards any direction along the horizontal plane.

Section 3 describes the hardware implementation, which consists of an RF beamformer, a dipole antenna array, and an experimental setup. Meanwhile, Section 4 discusses array analysis performance. To the best of the authors' knowledge, there are very few existing studies that combine all the above-mentioned techniques involved in the design of antenna arrays and RF beamforming systems. This article provides the reader a comprehensive study of RF beamforming systems using the induced EMF and GA methods, and whether or not they can be used, particularly in wireless applications.

2. Array Analysis and Optimization Technique

An adaptive beamforming technique is a complex system to implement in comparison with the switched beamforming technique. The adaptive beamforming technique requires the use of an advanced signal processing algorithm to steer the array's main beam in the direction of the signal of interest (SoI) while minimizing or nulling the array gain in the direction of the signals not of interest (SNoI). The beamforming weights (amplitude and phase) for each of the antenna elements are optimized using a combination of the genetic algorithm [22] and the induced EMF method [23–31] in order to direct the main beam in the direction of the SoI. The algorithm has been tested on a 2 by 2 dipole antenna array with a spacing of 0.9λ0 at 2.45 GHz. The genetic algorithm has been selected due to its robust characteristic, global optimization, and suitability for complex problems. On the other hand, the induced EMF method has been chosen as it provides a closed form solution to include the mutual coupling between the dipoles of antenna arrays.

2.1. The Induced EMF Method. The radiation pattern of an element depends on the impedance at each terminal. However, the condition stays valid when it is operating in an isolated environment. In a practical situation, the total radiation pattern of an array is largely influenced by mutual coupling between the neighboring elements. The total radiation pattern of the N elements of the half wavelength dipole antennas, E_{total}, can be calculated as [23]

$$E_{\text{total}}(\theta, \phi) = j\eta \left\{ \frac{\cos((\pi/2)\cos\theta)}{2\pi \sin\theta} \right\} \left\{ \sum_{n=1}^{N} \frac{I_n e^{-jkR_n}}{R_n} \right\}, \quad (1)$$

where the equation in the left bracket represents the radiation pattern of a half-wave dipole and the right bracket represents the array factor. I_n is the weight (amplitude and phase) that feed to each dipole, η is the wave impedance (120π), k is the wave number, and R_n refers to the distance between the observation point to each dipole in the antenna array.

The weights, I_n can be evaluated as in equations (2)–(4) [24] as

$$I_n = \left[Z^m + Z^s\right]^{-1} V^s, \quad (2)$$

where I_n is the current at nth dipole terminal, Z^m is the impedance matrix, and V^s and Z^s are the source voltage and load impedance for each element, respectively. Z^m includes the self (Z_{ii} : Z_{11}, Z_{22} until Z_{44}) and mutual impedance between the self and neighboring elements (Z_{ij}). The impedance matrices of Z^m and Z^s (50 Ω) are calculated in the following equations:

$$Z^m = \begin{bmatrix} Z_{11} & Z_{12} & \cdots & Z_{1N} \\ Z_{21} & Z_{22} & \cdots & Z_{2N} \\ \vdots & \vdots & \ddots & \vdots \\ Z_{N1} & Z_{N2} & \cdots & Z_{NN} \end{bmatrix}, \quad (3)$$

$$Z^s = \begin{bmatrix} 50 & 0 & \cdots & 0 \\ 0 & 50 & 0 & \vdots \\ \vdots & 0 & 50 & 0 \\ 0 & \cdots & 0 & 50 \end{bmatrix}. \quad (4)$$

The self and mutual impedance matrix is a square matrix with the order due to the size of an array. This signifies that the computation complexity increases with respect to the size of an array. However, there are several well-known estimation methods for finding the self and mutual

impedance of the wire-type antennas, such as the integral equation-moment method [25] and the induced electromotive force (EMF) method [26–30]. The induced EMF method provides a good approximation for calculating the mutual coupling and is easy to implement due to its closed form solution. King [29] described the computation method of self and mutual impedance, while Baker and LaGrone [30] conducted experimental validation of mutual impedance between the two half-wave dipoles.

The mutual impedance, $Z_{12,}$ is computed using the induced EMF method based on equations [29, 30]. The mathematical equation to compute the mutual impedance is derived as shown in equations (5) and (6) [30].

The results are shown in Figure 1 by varying the spacing between the two elements, d. It is observed that the magnitude of the mutual impedance of Z_{12} is inversely proportional to spacing. A good agreement can be observed between the equations [29, 30]. Its absolute values and phase are reflected as shown inthe equation[31].

In addition, Figure 1 shows that the magnitude of $|Z_{12}|$ decreases to zero as d increases. While its phase varies between -90° and 90°. On the other hand, the mutual resistance and reactance decrease gradually from positive to negative values as d increases. Mutual resistance and reactance can have positive or negative values depending on the frequency.

$$\begin{aligned} R_{21} = -30 \int_{t=-l_2/2}^{t=l_2/2} \Bigg\{ \Bigg[\frac{1}{\rho^2} \Bigg(& [\sin 2\pi r_1] \left[\frac{t_z + z_0 + l_1/2}{r_1} \right] + [\sin 2\pi r_2] \left[\frac{t_z + z_0 - (l_1/2)}{r_2} \right] \\ & - 2[\cos \pi l_1][\sin 2\pi r] \left[\frac{t_z + z_0}{r} \right] \Bigg) \left[t_x^2 + t_x x_0 + t_y y_0 + t_y^2 \right] \Bigg] \\ & + \left[\left(2 \frac{(\sin 2\pi r)(\cos \pi l_1)}{r} - \frac{\sin 2\pi r_1}{r_1} - \frac{\sin 2\pi r_2}{r_2} \right) t_z \right] \Bigg\} \left\{ \frac{\sin[2\pi(l_2/2 - |t|)]}{t} \right\} dt, \end{aligned} \tag{5}$$

$$\begin{aligned} X_{21} = -30 \int_{t=-l_2/2}^{t=l_2/2} \Bigg\{ \Bigg[\frac{1}{\rho^2} \Bigg(& [\cos 2\pi r_1] \left[\frac{t_z + z_0 + (l_1/2)}{r_1} \right] + [\cos 2\pi r_2] \left[\frac{t_z + z_0 - l_1/2}{r_2} \right] \\ & - 2[\cos \pi l_1][\cos 2\pi r] \left[\frac{t_z + z_0}{r} \right] \Bigg) \left[t_x^2 + t_x x_0 + t_y y_0 + t_y^2 \right] \Bigg] \\ & + \left[\left(2 \frac{(\cos 2\pi r)(\cos \pi l_1)}{r} - \frac{\cos 2\pi r_1}{r_1} - \frac{\cos 2\pi r_2}{r_2} \right) t_z \right] \Bigg\} \left\{ \frac{\sin[2\pi(l_2/2 - |t|)]}{t} \right\} dt, \end{aligned} \tag{6}$$

Equation (7) states the total dissipated power between the two conductors [32] as

$$P = \frac{1}{2} R_{11} |I_1|^2 + \frac{1}{2} R_{22} |I_2|^2 + R_{12} \mathrm{Re}(I_1 I_2^*). \tag{7}$$

Assuming that both I_1 and I_2^* are positive real numbers, a negative value of the mutual resistance would reduce the total power dissipation of the conductors.

2.2. Pattern Multiplication Method. The pattern multiplication method is a conventional technique to calculate the total radiation pattern of an array. It can be obtained by multiplying the array factor and radiation pattern of an element. However, it does not consider the mutual coupling effect between the neighboring elements. A program of mathematical analysis using pattern multiplication [28] has been written as compared with the induced EMF method. Figure 2 shows a comparison between both methods for 2 by 2 dipoles with spacing = 0.9 λ_0. It shows that there is a slight difference between them due to the coupling effect.

2.3. Genetic Algorithm. A genetic algorithm (GA) allows a set of chromosomes in a population to evolve toward a global optimum solution. GA consists of three major steps: selection, recombination, and mutation. GA is a search algorithm based on the process of natural selection and natural genetics [21, 33, 34]. To name a few, many works have employed GA in beamforming applications such as in pattern synthesis [35], array thinning [36], beam and null steering [37], multiobjective optimization [38], and element failure correction ability [39].

In this work, Figure 3 shows the desired main beam towards 100°–140° of SoI with a step size of 10° using the excitation weights of I_n (amplitude and phase). These angles are chosen due to the same spacing ($dx = dy$) of dipoles of this array [40]. Furthermore, as additional requirements to the optimization technique, a narrow beam of HPBW of 30° with side lobes of −10 dB is added. Five cosine-shaped beam patterns are designed as desired patterns, E_d in GA.

Considering the total radiation pattern of an antenna array as in equation (1), the optimization problem that GA is trying to maximize is displayed as [41]

$$f(x) = \frac{1}{1 + \sum_{i=1}^{Q} P_0 \left| E_{d_i} - E_{\mathrm{total}_i} \right|}, \tag{8}$$

where the fitness function, $f(x)$ is the absolute difference, Q is the total number of sampling points in the radiation pattern, P_0 is a scale constant which ranges from {0-1}, E_d is

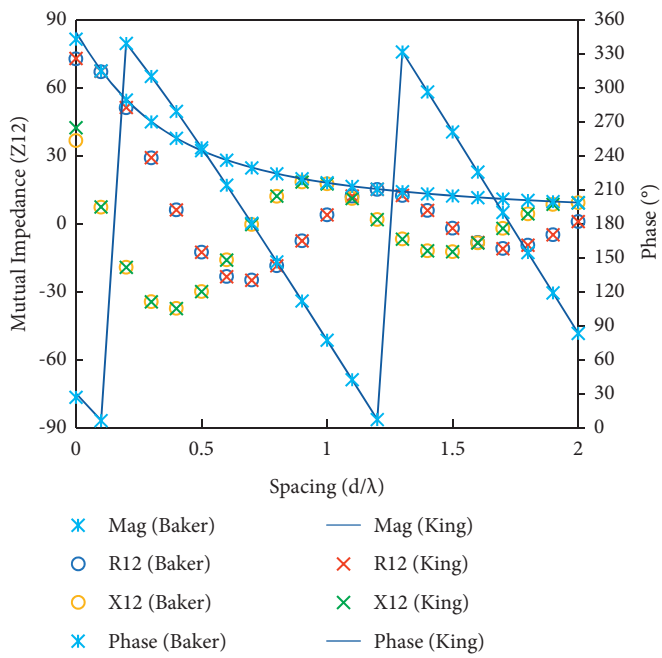

Figure 1: Mutual impedance between the two parallel dipole antennas with spacing d_0/λ_0.

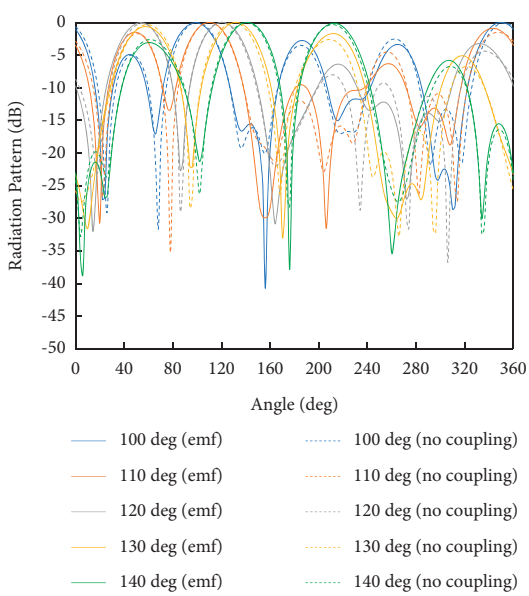

Figure 2: Comparison between pattern multiplication and the induced EMF methods (without GA) when steering the main beam towards 100°–140°.

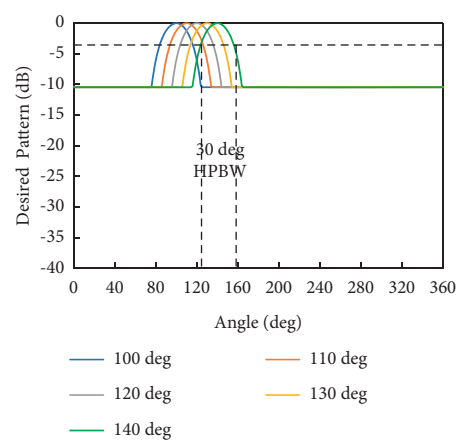

Figure 3: Desired SoI {100°–140°} with a step size of 10° in terms of the cosine-shaped beam pattern.

the desired radiation pattern, and E_{total} is the optimized radiation pattern of the GA and induced EMF method.

As a result, the total radiation pattern is optimized using the induced EMF and GA methods to meet the desired signal of interest (SoI) by varying the weights of I_n of the antenna elements.

2.4. Optimization Results. An optimization has been performed using a 2 by 2 dipole antenna array at 2.45 GHz with a spacing of $0.9\lambda_0$ (≈0.11 m). This section elaborates on the optimization results of the dipole antenna weights ($D1$, $D2$, $D3$, and $D4$) obtained using the induced EMF method and GA.

The SoI's of 100°–140° with a step size of 10° are chosen due to the fact that 2 by 2 dipoles are arranged in a symmetric position. Thus, by choosing this angle of interest, it enables the proposed optimization technique to be able to steer the beam in all directions along the azimuth plane of the dipole antenna array.

Figure 4 summarizes the optimization flow of the GA and the induced EMF method. The optimization process begins by defining the range of the weights parameters, I_n, and the desired radiation pattern. Then, GA initializes the random excitation weights (I_n) for $D1$, $D2$, $D3$, and $D4$ in the first population. The weights are calculated using equations (2)–(6) to include the mutual coupling effect. The

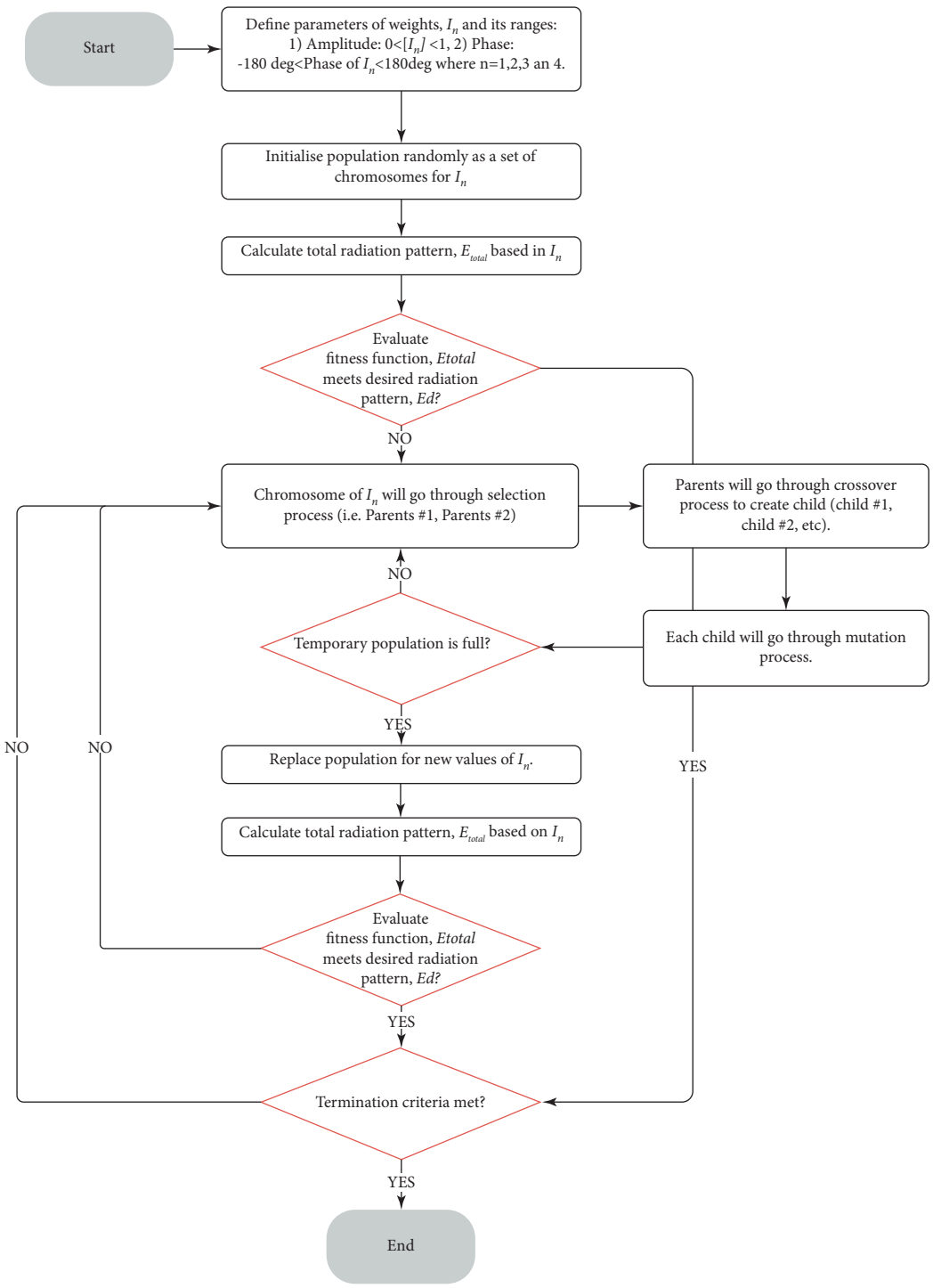

Figure 4: Flowchart of hybrid GA and the induced EMF method.

excitation weights, I_n, are represented in chromosomes. Next, the total radiation pattern, E_{total}, is computed using equation (1). Then, the fitness function between the total radiation pattern and the desired radiation pattern is computed using equation (8). The chromosome of excitation weights undergoes selection, crossover, and mutation processes in order to find a better fitness function. The process continues until the termination criterion has been met.

Figure 5 shows the result of the optimized radiation pattern by using a hybrid of the induced EMF and GA. The antenna array's SoI has been successfully steered towards 100°–140°. The results were verified with full-wave simulation software using the Empire XCCel. However, some differences in the radiation pattern can be seen at the side lobe and back lobe levels. The differences could be attributed to the limited number of step angles calculated by using the induced EMF method compared to the empire

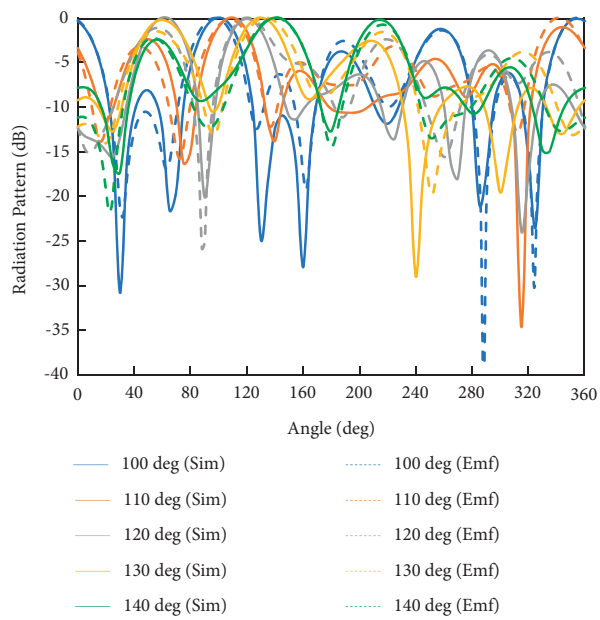

Figure 5: Optimized radiation pattern of 100°–140° using the induced EMF method and genetic algorithm (solid lines). The results were verified with the full-wave simulation software (dashed lines).

Table 1: The excitation weight, I_n, for each dipole element.

SoI	100°	110°	120°	130°	140°
$D1$	0.4 (100°)	1.00 (310°)	0.50 (100°)	0.50 (18°)	0.80 (220°)
$D2$	0.30 (175°)	0.70 (5°)	0.55 (225°)	0.50 (175°)	0.90 (55°)
$D3$	0.50 (180°)	1.00 (107°)	0.88 (330°)	0.60 (340°)	0.50 (260°)
$D4$	0.25 (134°)	0.65 (320°)	0.75 (122°)	0.86 (110°)	1.00 (360°)

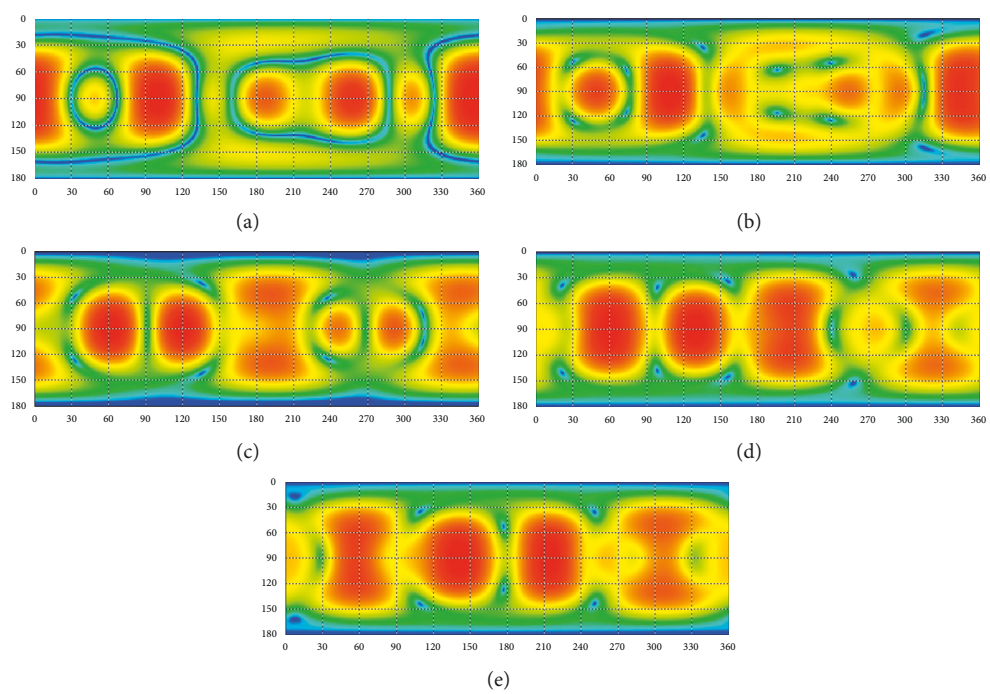

Figure 6: 2D radiation pattern of optimized beams at: (a) 100°, (b) 110°, (c) 120°, (d) 130°, and (e) 140°.

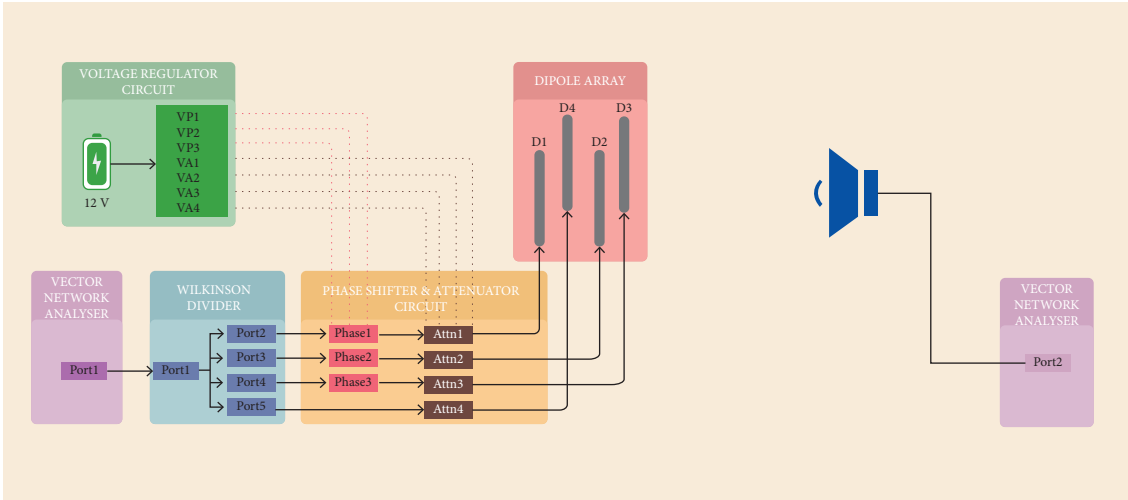

Figure 7: A block diagram of the dipole antenna array and its RF beamformer circuit as the transmitter and horn antenna as the receiver.

XcCel. This is done to make the optimization process more manageable and less time-consuming by using MATLAB. It is also observed that the optimized pattern with GA is better than the radiation patterns in Figure 2 (without GA), especially in the side lobe region. Meanwhile, Table 1 refers to the optimized value of excitation weights, $I_{n,}$ for the radiation pattern plotted in Figure 5. Figure 6 shows the optimized radiation pattern in 2D in Figure 6(a) 100°, Figure 6(b) 110°, Figure 6(c) 120°, Figure 6(d) 130°, and Figure 6(e) 140°.

3. Experimental Setup

Figure 7 depicts the flow of an RF beamformer system and a dipole antenna array. The experimental setup consists of a voltage regulator circuit, a signal generator, a Wilkinson divider, an attenuator, a phase shifter circuit, and a dipole antenna array. It also consists of a signal generator where port 1 generates the RF signal through the RF beamformer and the dipole array. The generated signal divides itself into four equal output signals by using the Wilkinson divider, and then they are routed through the attenuator and the phase shifter circuit.

Finally, the attenuator and the phase shifter circuit are used to control the weights, $I_{n,}$ of each of the dipoles ($D1$, $D2$, $D3$, and $D4$). On the right-hand side, the horn antenna receives the transmitted signal. The strength signal is then measured by using a spectrum analyzer.

3.1. Voltage Regulator Circuit. Figure 8 represents the voltage regulator circuit to supply the DC voltage (V_{p1}, V_{p2}, V_{p3}, V_{a1}, V_{a2}, $V_{a3,}$ and V_{a4}) to the phase shifter (JHPHS 2484+) and the attenuator (EVA 3000+) surface mount device (SMD) as mentioned in part C. In addition, the voltage regulator circuit (V_{pm} and V_{an}, m and n is the index of the phase shifter and attenuator) has been tuned to produce the desired excitation weights, $I_{n,}$ of the dipole antennas.

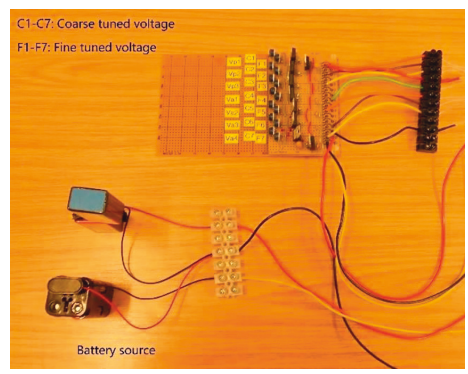

Figure 8: Voltage regulator circuit.

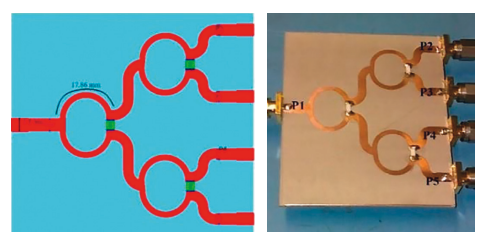

(a) (b)

Figure 9: (a) The design of a 4 : 1 Wilkinson divider and (b) the fabrication of the 4 : 1 Wilkinson divider [43].

3.2. Wilkinson Divider. A 4 : 1 Wilkinson divider [42] at 2.45 GHz is designed to divide the RF signal equally with the same phase as an input to a dipole array (Figure 9(a)). Then, the design is fabricated on 1.524 mm thick Rogers/Duroid 6002 with a dielectric constant of 2.94 and a loss tangent of 0.0012 (Figure 9(b)).

3.3. Phase Shifter and Attenuator Circuit. The azimuth beam steering is achieved by using the phase shifter and the attenuator circuit as shown in Figure 10. V_{p1} and V_{a1} are varying voltages (0–15 V) and (0–8 V) for the phase shifter

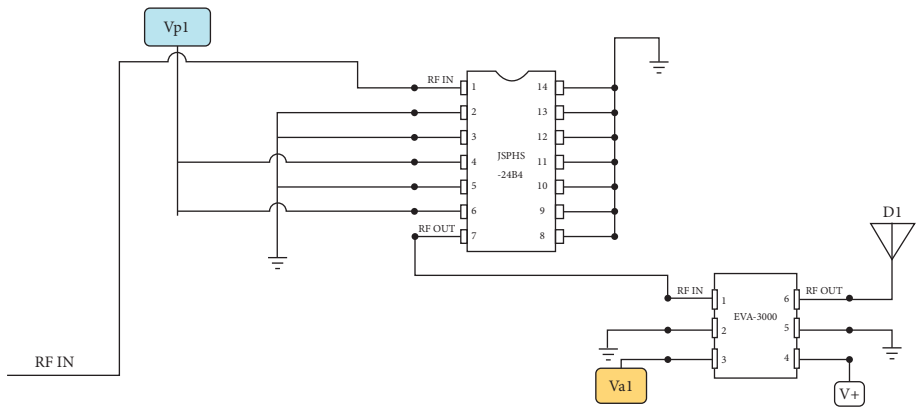

Figure 10: A schematic diagram of a single way SMD phase shifter and attenuator.

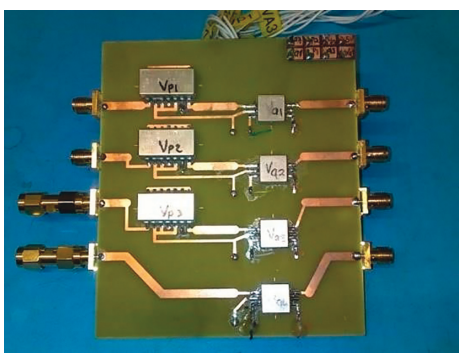

Figure 11: Phase shifter and attenuator circuit [43].

Table 2: Dimensions of dipole antennas [43].

Dipole no.	Length (mm) with 2 mm feed gap	Diameter (mm)
$D1$	52.73	2.06
$D2$	53.12	2.06
$D3$	53.55	2.06
$D4$	53.12	2.06

and the attenuator for the first branch of the circuit. While V_{p2}, V_{a2} and V_{p3}, V_{a3} refer to the second and third phase shifter and attenuator, respectively. Lastly, V_{a4} refers to the fourth attenuator in the circuit. A set of 3 phase shifters [44] and 4 attenuators [45] are controlled by the voltage regulator circuit. The aim is to provide 45 states of phase (with $\Delta\varphi = 5.98^{\circ}$) and 32 states of attenuation (with a maximum attenuation of 35 dB). The prototype of the circuit is shown in Figure 11. The copper track is etched on FR4 with a thickness of 2.54 mm. The 24 V battery acts as a supply voltage for both chips via 5 m of thin cables. The long cables allow the feed network to rotate along with the antenna array during the radiation pattern measurement.

3.4. Dipole Antenna. Four dipole antennas with the dimensions shown in Table 2 were designed using the Empire XCCel (Figures 12(a) and 13). Later, the dipole antennas with balun [46] were constructed using the RG-58/U coaxial cable and were soldered to the male SMA connectors (Figure 12(b)).

(a) (b)

Figure 12: (a) Simulation design of a dipole antenna and (b) the fabrication of dipole antennas [43].

3.5. Integrated Antenna with RF Beamformer Circuit. Next, all dipole antennas are arranged in the planar with the Rohacell material as the antennas' supporting structure (Figure 14(a)). The spacing between the dipole antennas is 0.11 m ($0.9\lambda_0$). The reason we chose $0.9\lambda_0$ is due to the minimum spacing that can be constructed by considering the length of the balun (as shown in Figure 14(b)). Figure 15 depicts the antenna array and beamformer circuit assembly. Figure 16(a) portrays a measurement setup representing radiation where the dipole array and the beamformer circuit act as transmitters, and figure 16(b) shows the horn antenna as the receiver.

4. Design Performance Analysis

4.1. Voltage Regulator, Attenuator, and Phase Shifter Circuits. Several investigations have been carried out using a spectrum analyzer in order to study the characteristics of the phase shifter and the attenuator circuit (i.e., phase, $\varnothing_p$ and attenuation, A_q) compared to the controlled voltage of the phase shifter and attenuator, V_{pp} and V_{aq}. The values of p and q are the number of phase shifters and attenuators, respectively, where $p = 1, 2, 3$ and $q = 1, 2, 3, 4$.

Figure 17 depicts the phase of each output channel, $\varnothing_p$, as the controlled voltage of the phase shifter, V_{pp}, varies from 0–15 V. The attenuator's voltage, V_{aq}, has been kept constant. It shows that the phase for each output channel (CH1, CH2, and CH3) increases as the V_{pp} varies from 0 to 15 V. Figure 18 shows the phase of each output channel, $\varnothing_p$, as the controlled voltage of the attenuator, V_{aq}, varies from 0 to

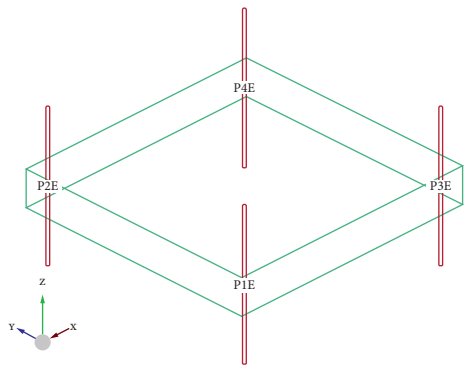

Figure 13: Simulation design of a dipole antenna array [43].

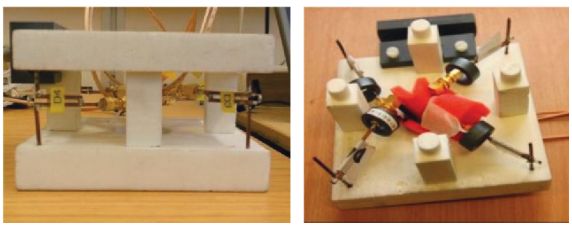

(a) (b)

Figure 14: Rohacell material has been constructed as the supporting structure to the antenna array (a) side view and (b) the top view.

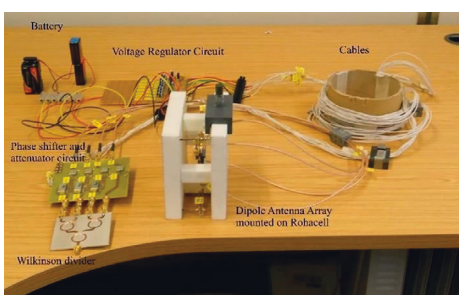

Figure 15: An assembly of a dipole antenna array and an RF beamformer circuit.

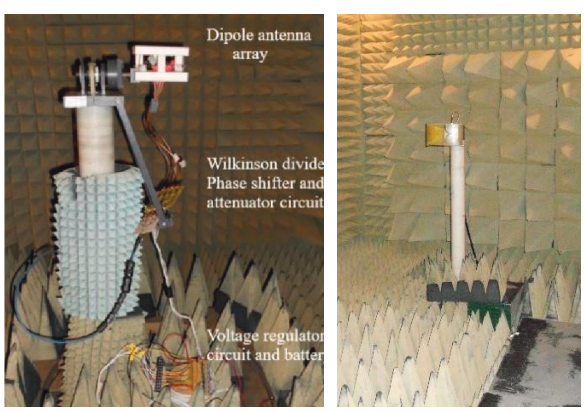

(a) (b)

Figure 16: (a) Measurement setup of the dipole array and the RF beamformer circuit (transmitter) and (b) the horn antenna (receiver).

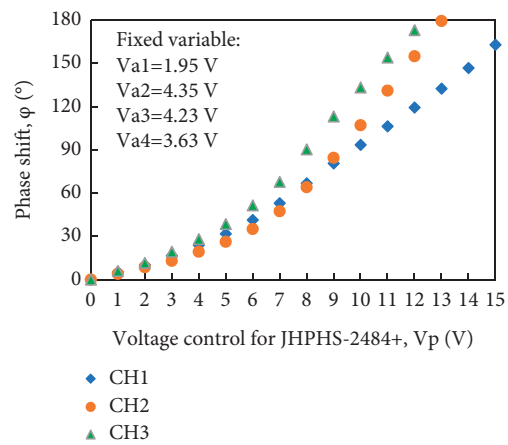

Figure 17: Output phase, $ø_{p,}$ of each channel when V_{pp} varies from 0–15 V and V_{aq} is kept constant.

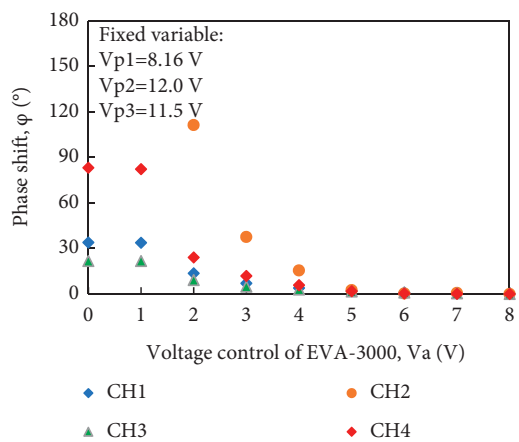

Figure 18: Output phase, $ø_{p,}$ of each channel when V_{aq} varies from 0 to 8 V and V_{pp} is kept constant.

8 V. The phase shifter's voltage, V_{pp}, has been held constant. It has been discovered that as V_{aq} increases, the phase of each output channel decreases to zero degrees.

Figure 19 represents the attenuation of each output channel, A_q, as the phase shifter's controlled voltage, $V_{pp,}$ varies from 0 to 15 V. The controlled voltage of the attenuator, $V_{aq,}$ has been kept constant. Thus, the attenuation loss has remained constant for all channels, with the exception of a small increase in attenuation at CH2, when V_{pp} increases from 10 to 15 V.

On the other hand, Figure 20 displays the attenuation of each output channel, A_q, as the controlled voltage of the attenuator, V_{aq}, varies from 0 to 8 V. The phase shifter's controlled voltage, V_{pp}, is held constant, and when the V_{aq} increases from 0 to 8 V, the attenuation loss for all channels decreases.

4.2. Wilkinson Divider. The simulation and measurement results of the S-parameters of S_{12}, S_{13}, S_{14}, and S_{15} are shown in Figure 21. The graph shows that the insertion loss of the measurement results matches the simulation results at 2.45 GHz, with values around 6 dB.

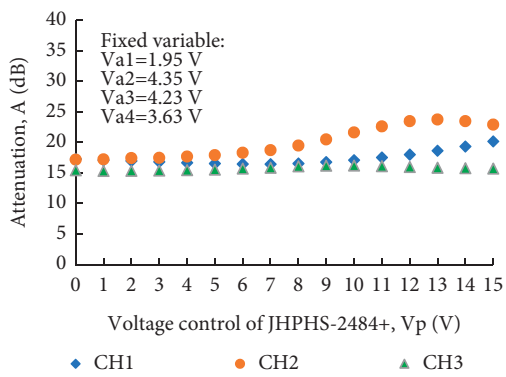

Figure 19: Attenuation, A_q, of each channel when V_{pp} varies from 0–15 V and V_{aq} is kept constant.

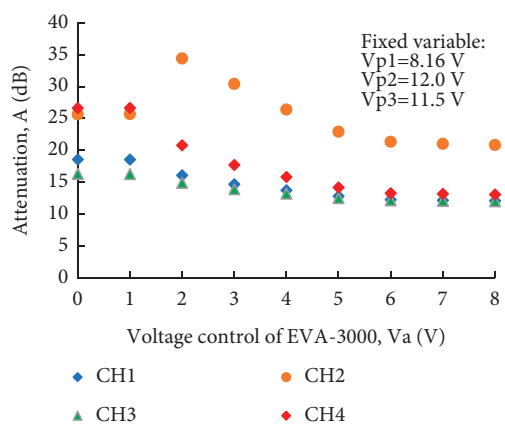

Figure 20: Attenuation, A_q, of each channel when V_{aq} varies from 0 to 8 V and V_{pp} is kept constant.

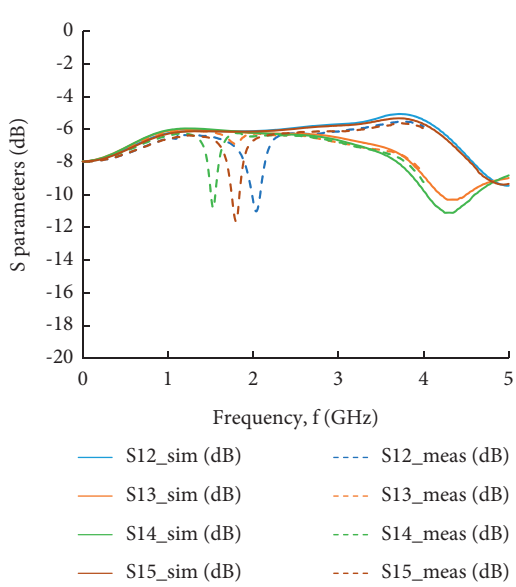

Figure 21: Simulation (dashed lines) and measurement (solid lines) magnitude of S_{12}, S_{13}, S_{14}, S_{15}, of the Wilkinson divider.

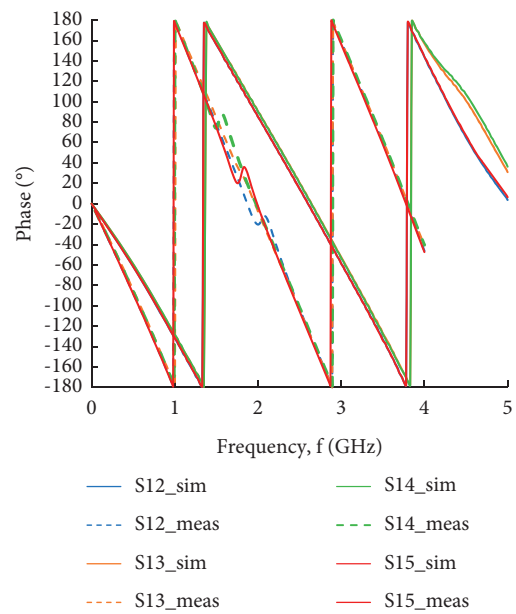

Figure 22: Simulation (dashed lines) and measurement (solid lines) phase of S_{12}, S_{13}, S_{14}, S_{15}, of the Wilkinson divider.

Figure 22 depicts the phase of S-parameters. It was discovered that there is a 110° phase difference between the simulated and measured results. It could be due to the extra length of the copper added on the top of FR4 during the soldering process of an internal resistor and SMA connectors, which is not considered in simulation. However, the simulation and measurement phases between all ports are almost similar. Thus, the measurement results ensure that each port's output signals are in a similar phase with each other, which meets the desired specifications of the Wilkinson divider.

4.3. Dipole Antennas. Figure 23 represents the simulation and measurement results of S_{11} for $D1$, $D2$, $D3$, and $D4$. It is observed that there is a small difference between the measurement and simulation results. A small difference can be noted when the resonant frequencies for the measured plots are shifted to higher frequencies than the simulated plots. However, all the measured S_{11s} are less than −10 dB at 2.45 GHz. This is because the dipoles are fabricated using the cut-and-try approach during S_{11} measurement. The cause is that the fabricated antenna has experienced some tolerance error due to man-made fabricating and assembling.

Furthermore, the simulation model (Figure 12(a)) does not resemble the practical design of a dipole, as shown in Figure 12(b). Moreover, the dipole antenna's thin diameter (2.06 mm) makes it prone to breaking during measurement. Figure 23 shows that $D2$ has the best measured S_{11} at 2.45 GHz, with a value of −13.47 dB, when compared to $D1$, $D3$, and $D4$.

4.4. S_{11} and Radiation Pattern of Array with RF Beamformer. Finally, the RF beamformer and dipole array have been assembled in an anechoic chamber for the radiation pattern

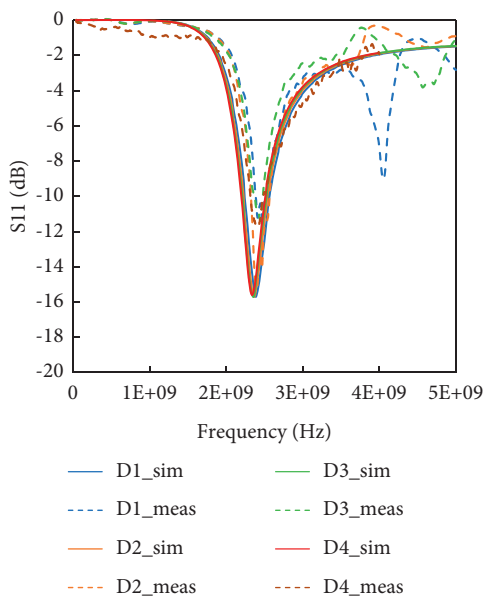

Figure 23: Simulation (solid lines) and measurement (dashed lines) results of S_{11} parameters of $D1$, $D2$, $D3$, and $D4$.

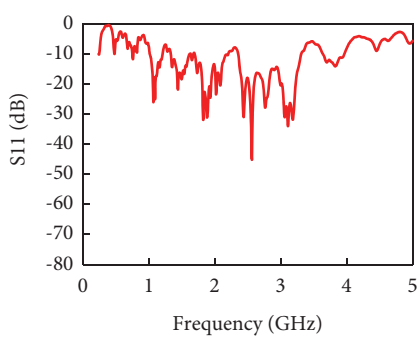

Figure 24: Measurement result of the S_{11} parameter for the whole system [43].

measurement. The measurement of S_{11} parameters of the whole system (dipole array and beamformer circuit) is shown in Figure 24. It is observed that the initial resonant frequency at 2.45 GHz has been shifted to 2.56 GHz.

Therefore, a few samples of the radiation pattern of the system have been measured at three frequencies; 2.45 GHz, 2.54 GHz, and 2.56 GHz. Table 3 represents the excitation weights, I_n values for each dipole. The comparison of the simulated and measured radiation patterns of the entire system array is shown in Figure 25. It is observed that there is an agreement within the main lobe between simulated and measured results at 2.56 GHz compared to other frequencies. The range of agreement is within 0–120°.

In summary, Table 4 compares the introduced antenna design's performance with other published works [14–21]. As can be seen, this work meets the objective of steering the main beam in any direction in the horizontal plane. The contribution of this work refers to the array analysis by using the conventional technique of the hybrid induced EMF method combined with GA. It has been verified with

Table 3: The weights of each element of the dipole antenna.

	2.45 GHz	2.56 GHz	2.59 GHz
$D1$	0.05 (−95°)	0.15 (112°)	0.14 (−155°)
$D2$	0.20 (−116°)	0.17 (−140°)	0.18 (−150°)
$D3$	0.16 (−82°)	0.12 (−145°)	0.12 (−155°)
$D4$	0.17 (17°)	0.10 (−150°)	0.11 (−160°)

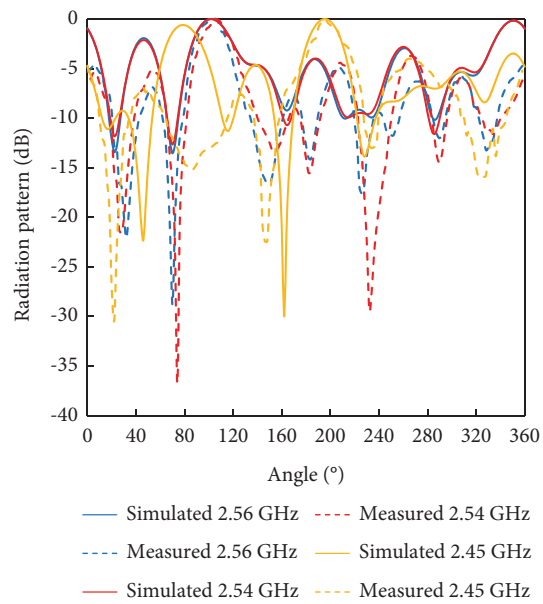

Figure 25: Simulation (solid lines) and measurement (dashed lines) results of the radiation patterns of the dipole antenna array and RF beamformer circuit.

hardware implementation at 2.56 GHz. Even though some discrepancies existed between the simulation and measurement results, it still shows the reliability and relevance of the conventional techniques in wireless communication, particularly WLAN and 5G.

5. Limitation of the Study

The induced EMF method is a conventional technique to calculate the mutual impedance between the two terminals of the dipole antennas in an array. Although conventional, it provides a closed-form solution for the computation of the coupling matrix. Furthermore, its absolute values $|Z_{mn}|$ have been verified with the experimental work as presented in [26]. On the other hand, full-wave simulation such as the FDTD method is highly sensitive to numerically large ranges of structural dimensions, which does not apply to very thin dipole (relative to its length) antennas [47]. Moreover, another challenge is the excitation definition of the finite gaps for dipoles. Full-wave simulation uses ports as excitation voltage while the induced EMF method uses the current distribution to calculate the dipole impedance, which is accurate in this research. Thus, this research is only applicable to wire dipole antennas with dimension limitations of the length, $l < 0.8\lambda$ and radius, $a < 10^{-2}\lambda$, as explained in [47].

Table 4: Comparison of this work and previous works.

Reference	Algorithm	Antennas type/ no. of elements	Antennas configuration	Hardware implementation	Objectives
[14]	Ambiguity function analysis equation and genetic algorithm	(i) Patch antennas (ii) 4 TX (iii) 8 RX	(i) 0.5λ spacing (ii) Planar array	Yes, at 76.5 GHz	To optimize antenna position in order to obtain ambiguity in the direction of arrival estimation
[15]	HFSS and genetic algorithm	(i) Multiring dielectric lens antennas (ii) 4 index	(i) Feed spacing of 0.5λ spacing.	Yes, at 38 GHz	To reduce the adjacent beam transition region for beam stability at mmW frequencies, by varying lens permittivity and ring size
[16]	Array factors and improved chicken swarm optimization (ICSO)	(i) Isotropic (ii) 16 and 64 elements	(i) Linear array (ii) Circular array (iii) Random array	No	To reduce maximum side lobe level by varying weight excitations (SLL).
[17]	Memetic method: GA and quasi-Newton method	(i) Patch antenna (ii) 2 by 2 (iii) 8 by 8 (iv) 16 by 16	(i) Planar array (ii) 0.5λ spacing	No	Minimize return loss (S_{11}).
[18]	Cross correlation green function and GA	(i) Dipole antennas	(i) Circular (ii) Cubic (iii) Conformal array	No	Synthesizing surface or volume MIMO antenna arrays with optimum cross correlation diversity gain performance (>80%) (varying space and orientation)
[19]	Improved harmony search algorithm (IHSA) and array factor	(i) Isotropic elements (ii) 16 and 30	(i) Time modulated linear array (TMLA) (ii) 0.5λ spacing	No	To optimize pulse shifting, excitations in timed antenna array for the reduction of sidelobe and sideband
[20]	MoM (CST) and social network optimization (SNO)	(i) Reflect array antenna (ii) 24 by 24	(i) Planar	No	To scan the beam over a predefined angular range [θs min, θs max] in the elevation plane
[21]	Embedded pattern and particle swarm optimization	(i) Patch antenna	(i) Linear (ii) 0.5λ spacing	Yes, at 7 GHz	To steer the beam to 0°, 30°, and 45° from broadside with maximum SLL of 20 d while compensating broken elements
This work	Induced EMF method and GA	(i) λ/2 dipole antenna (ii) 2 by 2	(i) Planar array (ii) 0.9λ0 spacing	Yes, at 2.45 GHz	Steer the 30° HPBW main beam along the azimuth (horizontal) plane with step size of 10° and −10 dB SLL

6. Conclusion

In this paper, an analysis and optimization of the dipole antenna array have been conducted by using a combination of the induced EMF and genetic algorithm methods. The results have been verified with full-wave simulation software, and the results are in good agreement with each other. In order to realize an adaptive beamforming system, an RF beamformer circuit consisting of a voltage regulator circuit, a Wilkinson divider, a phase shifter, an attenuator circuit, and a dipole antenna array have been designed and assembled. The measurement result of S_{11} of the whole system shows some displacement of the resonant frequency from 2.45 GHz to 2.56 GHz. However, the simulation and measurement of the radiation pattern of the beam steering antenna array are in agreement with each other, which validates this research.

Data Availability

The data are available from the corresponding author upon request (norun@iium.edu.my).

Conflicts of Interest

The authors declare that they have no conflicts of interest.

Authors' Contributions

Equal contributions were made by each author.

Acknowledgments

This work was partially supported by the Ministry of Education, Malaysia (under grant FRGS/1/2018/ICT03/UIAM/02/2) and International Islamic University Malaysia.

References

[1] M. R. Akdeniz, Y. Liu, M. K. Samimi et al., "Millimeter wave channel modeling and cellular capacity evaluation," *IEEE Journal on Selected Areas in Communications*, vol. 32, no. 6, pp. 1164–1179, 2014.

[2] A. M. Al-Saman, M. Cheffena, M. Mohamed, M. H. Azmi, and Y. Ai, "Statistical analysis of rain at millimeter waves in tropical Area," *IEEE Access*, vol. 8, pp. 51044–51061, 2020.

[3] T. S. Rappaport, F. Gutierrez, E. Ben-Dor, J. N. Murdock, Y. Qiao, and J. I. Tamir, "Broadband millimeter-wave propagation measurements and models using adaptive beam antennas for outdoor urban cellular communications," *IEEE Transactions on Antennas and Propagation*, vol. 61, no. 4, pp. 1850–1859, 2013.

[4] W. Roh, J.-Y. Seol, J. Park et al., "Millimeter-wave beamforming as an enabling technology for 5G cellular communications: theoretical feasibility and prototype results," *IEEE Communications Magazine*, vol. 52, no. 2, pp. 106–113, Feb. 2014.

[5] S. Rangan, T. S. Rappaport, and E. Erkip, "Millimeter-wave cellular wireless networks: potentials and challenges," *Proceedings of the IEEE*, vol. 102, no. 3, pp. 366–385, Mar. 2014.

[6] H. Q. Ngo, E. G. Larsson, and T. L. Marzetta, "Energy and spectral efficiency of very large multiuser MIMO systems," *IEEE Transactions on Communications*, vol. 61, no. 4, pp. 1436–1449, 2013.

[7] F. Rusek, D. Persson, B. K. Lau et al., "Scaling up MIMO: opportunities and challenges with very large arrays," *IEEE Signal Processing Magazine*, vol. 30, no. 1, pp. 40–60, 2013.

[8] S. Han, I. Chih-Lin, Z. Xu, and C. Rowell, "Large-scale antenna systems with hybrid analog and digital beamforming for millimeter wave 5G," *IEEE Communications Magazine*, vol. 53, no. 1, pp. 186–194, 2015.

[9] Y. Sun and C. Qi, "Weighted sum-rate maximization for analog beamforming and combining in millimeter wave massive MIMO communications," *IEEE Communications Letters*, vol. 21, no. 8, pp. 1883–1886, 2017.

[10] R. Hu, L. Jiang, and P. Li, "Hybrid beamforming with deep learning for large-scale Antenna arrays," *IEEE Access*, vol. 9, pp. 54690–54699, 2021.

[11] S. Zhang, C. Guo, T. Wang, and W. Zhang, "ON–OFF analog beamforming for massive MIMO," *IEEE Transactions on Vehicular Technology*, vol. 67, no. 5, pp. 4113–4123, 2018.

[12] G. Zhou, "Energy efficiency beamforming design for UAV communications with broadband hybrid polarization antenna arrays," *IEEE Access*, vol. 7, pp. 34521–34532, 2019.

[13] M. M. Kamal, S. Yang, X.-cheng Ren et al., "Infinity shell shaped MIMO antenna array for mm-wave 5G applications," *Electronics*, vol. 10, no. 2, p. 165, 2021.

[14] A. Di Serio, P. Hügler, F. Roos, and C. Waldschmidt, "2-D MIMO radar: a method for array performance assessment and design of a planar antenna array," *IEEE Transactions on Antennas and Propagation*, vol. 68, no. 6, pp. 4604–4616, June 2020.

[15] H. T. Chou, Y. S. Chang, H. J. Huang, Z. D. Yan, T. Lertwiriyaprapa, and D. Torrungrueng, "Two-dimensional multi-ring dielectric lens antenna to radiate fan-shaped multi beams with optimum adjacent-beam overlapping crossover by genetic algorithm," *IEEE Access*, vol. 8, pp. 79124–79133, 2020.

[16] S. Liang, Z. Fang, G. Sun, Y. Liu, G. Qu, and Y. Zhang, "Sidelobe reductions of antenna arrays via an improved chicken swarm optimization approach," *IEEE Access*, vol. 8, pp. 37664–37683, 2020.

[17] X. Zhang, M. Lin, X. Zhang, and Y. Li, "The design of microstrip array antenna and its optimization by a memetic method," *IEEE Access*, vol. 7, pp. 96434–96443, 2019.

[18] S. M. Mikki, S. Clauzier, and Y. M. M. Antar, "Empirical geometrical bounds on MIMO antenna arrays for optimum diversity gain performance: an electromagnetic design approach," *IEEE Access*, vol. 6, pp. 39876–39894, 2018.

[19] A. Chakraborty, G. Ram, and D. Mandal, "Optimal pulse shifting in timed antenna array for simultaneous reduction of sidelobe and sideband level," *IEEE Access*, vol. 8, pp. 131063–131075, 2020.

[20] A. Niccolai, M. Beccaria, R. E. Zich, A. Massaccesi, and P. Pirinoli, "Social network optimization based procedure for beam-scanning reflectarray antenna design," *IEEE Open Journal of Antennas and Propagation*, vol. 1, pp. 500–512, 2020.

[21] L. A. Greda, A. Winterstein, D. L. Lemes, and M. V. T. Heckler, "Beamsteering and beamshaping using a linear antenna array based on particle swarm optimization," *IEEE Access*, vol. 7, pp. 141562–141573, 2019.

[22] J. H. Holland, *Adaptation in Natural and Artificial Systems*, University of Michigan Press, Ann Arbor, MI, 1975.

[23] C. A. Balanis, *Linear Wire Antennas" in Antenna Theory: Analysis and Design*, Wiley-Interscience, New York, Third edition, Chapter 4, pp. 151–219, 2005.

[24] W. L. Stutzman and G. A. Thiel, *Arrays" in Antenna Theory and Design*, Wiley & Sons, New York, Second edition, Chapter 3, pp. 87–142, 1998.

[25] G. A. Thiele, "Analysis of yagi-uda type Antennas," *IEEE Transactions on Antennas and Propagation*, vol. 17, no. 1, pp. 24–31, 1969.

[26] L. Lewin, "Mutual impedance of wire aerial," *Wireless Engineer*, vol. 28, Article ID 352355, 1951.

[27] K. E. Schmidt, "Simplified mutual impedance of nonplanar skew dipoles," *IEEE Transactions on Antennas and Propagation*, vol. 44, no. 9, pp. 1298-1299, 1996.

[28] J. Richmond and N. Geary, "Mutual impedance of nonplanar-skew sinusoidal dipoles," *IEEE Transactions on Antennas and Propagation*, vol. 23, no. 3, pp. 412–414, 1975.

[29] H. E. King, "Mutual impedance of unequal length antennas in echelon," *IRE Transactions on Antennas and Propagation*, vol. 5, no. 3, pp. 306–313, July 1957.

[30] H. Baker and A. LaGrone, "Digital computation of the mutual independance between thin dipoles," *IRE Transactions on Antennas and Propagation*, vol. 10, no. 2, pp. 172–178, 1962.

[31] H. Singh, H. L. Sneha, and R. M. Jha, "Mutual coupling in phased arrays: a review," *International Journal of Antennas and Propagation*, vol. 2013, Article ID 348123, 2013.

[32] J. E. Bracken, "Mutual resistance in spicelink," Ph.D. Ansoft Corporation, 2000.

[33] A. S. Fraser, "Simulation of genetic systems by automatic digital computers. II: effects of linkage on rates under selection," *Australian Journal of Biological Sciences*, vol. 10, no. 4, pp. 492–499, 1957.

[34] H. J. Bremermann, "The evolution of intelligence," in *The Nervous System as a Model of its Environment*Technical

Report No. 1, Department of Mathematics, University of Washington, Seattle, WA, 1958.

[35] S. I. Farghaly, H. E. Seleem, M. M. Abd Elnaby, and A. H. Hussein, "Pencil and shaped beam patterns synthesis using a hybrid GA/l_1 optimization and its application to improve spectral efficiency of massive MIMO systems," *IEEE Access*, vol. 9, pp. 38202–38220, 2021.

[36] A. Mohan and A. A. B. Raj, "Array thinning of beamformers using simple genetic algorithm," in *Proceedings of the International Conference on Computational Intelligence for Smart Power System and Sustainable Energy (CISPSSE)*, pp. 1–4, IEEE, Keonjhar, India, July 2020.

[37] A. Hamza and H. Attia, "Fast beam steering and null placement in an adaptive circular antenna array," *IEEE Antennas and Wireless Propagation Letters*, vol. 19, no. 9, pp. 1561–1565, Sept. 2020.

[38] G. Sun, X. Zhao, G. Shen et al., "Improving performance of distributed collaborative beamforming in mobile wireless sensor networks: a multiobjective optimization method," *IEEE Internet of Things Journal*, vol. 7, no. 8, pp. 6787–6801, 2020.

[39] X. Jiang, J. Qin, and T. Jiang, "Comparing the failure correction ability between GA and fa for array antenna," in *Proceedings of the 2019 Joint International Symposium on Electromagnetic Compatibility, Sapporo and Asia-Pacific International Symposium on Electromagnetic Compatibility (EMC Sapporo/APEMC)*, pp. 737–740, IEEE, Sapporo, Japan, November 2019.

[40] N. A. Malek, R. D. Seager, and J. A. Flint, "Beam steering of four dipoles antenna array using genetic algorithm," in *Proceedings of the 2014 IEEE Symposium on Wireless Technology and Applications (ISWTA)*, pp. 146–151, IEEE, Kota Kinabalu, Malaysia, October 2014.

[41] S. O. Kundukulam and K. S. Beenamole, "Design of a linear array antenna for shaped beam using genetic algorithm," *International Journal of RF and Microwave Computer-Aided Engineering*, vol. 18, no. 5, pp. 410–416, 2008.

[42] E. J. Wilkinson, "An N-way hybrid power divider," *IEEE Transactions on Microwave Theory and Techniques*, vol. 8, no. 1, pp. 116–118, Jan. 1960.

[43] N. F. A. Malek, *3-D Antenna Array Analysis Using the Induced EMF Method*, Ph.D. dissertation, School of Electronic, Electrical and Software Engineering, Loughborough University, Loughborough. UK, 2013.

[44] Mini Circuits, "surface mount voltage variable attenuator, EVA-3000+," Brooklyn: NY, 2021, https://www.minicircuits.com/pdfs/EVA3000+.pdf.

[45] Mini Circuits, "surface mount phase shifter, JHPHS-2484+," Brooklyn: NY, 2021, https://www.minicircuits.com/pdfs/JSPHS2484+.pdf.

[46] W. K. Roberts, "A New wide-band balun," *Proceedings of the IRE*, vol. 45, no. 12, pp. 1628–1631, 1957.

[47] M. Dehghani Estarki, Y. Xing, Xu Han, and R. G. Vaughan, "The effect of gap size on dipole impedance using the induced EMF method," in *Proceedings of the 2010 URSI International Symposium on Electromagnetic Theory*, pp. 373–376, IEEE, Berlin, August 2010.